Multiple sources of variability drive a stochastic cell fate decision in *C. elegans*

Jason R. Kroll, Jasonas Tsiaxiras, and Jeroen S. van Zon*

AMOLF, Amsterdam, 1098 XG, The Netherlands
*corresponding author

Abstract

Stochastic cell fate decisions occur frequently during animal development. In many cases, individual cells randomly choose one cell fate out of a limited repertoire of fates, but with the relative frequency of the different possible fates tightly controlled. It is not understood how signaling networks enable such cell-autonomous stochastic decisions and what network properties control the relative frequency of the resulting cell fates. To address these questions, we studied the differentiation of the *C. elegans* P3.p cell as a model system for a cell-autonomous stochastic cell fate decision. We use a novel time-lapse microscopy technique to measure the single-cell dynamics of BAR-1/β-catenin and LIN-39/Hox, two key regulators of the network, while monitoring both the timing and outcome of the decision. Surprisingly, the timing of the decision is highly regulated, even in mutants that drastically alter the frequency of the cell fates. Using experimental data and modeling approaches, we find that a combination of variability in LIN-39 levels and variability in the timing of BAR-1/β-catenin signaling are noise sources that bias the stochastic decision. Our results highlight that a novel aspect of Wnt signaling can provide sufficient variation in a signaling network to enable a cell-autonomous stochastic cell fate decision in a multicellular organism.

Introduction

During development, gene expression is highly regulated in order to enable our cells to adopt their correct developmental fate and function. While most cellular decisions are specified following a highly stereotypical developmental pattern, some cell fate decisions are stochastic and cells choose between multiple fate outcomes, often at a defined frequency (Elowitz et al., 2002; Losick and Desplan, 2008; Raj et al., 2010). Little is known about how the outcome of the stochastic decisions could be tuned or regulated, but some models suggest that noise or variability in regulators works its way through a genetic network to eventually create a bimodal distribution of cell-fate determination molecules (Fig. 1a).

Noisy gene expression has been identified as the source of variation responsible for many alternate cell fates in single-cell organisms. One of the early examples is the finding that intrinsic noisy gene expression in the master regulator of cell competence, *comK*, regulates the cell fate in *Bacillus subtilis* (Maamar et al., 2007). In independent cultures of *B. subtilis*, a small portion of the population becomes antibiotic-resistant (Balaban, 2004; Losick and Desplan, 2008). This small portion of the population, called “persisters”, stochastically arises from the adoption of a different set of expression levels in genes that control a toxin and anti-toxin, effectively becoming “trapped” in a quiescent yet antibiotic-resistant state. These results indicate that noisy gene expression is a sufficient mechanism to produce the bimodality that leads to different stochastic cell fates (Kearns and Losick, 2005; Losick and Desplan, 2008).

Developmental cell fate decisions in multicellular organisms are more complicated than single-celled organisms due to the interactions of other cells, the influence of signaling networks, and temporal constraints of developmental events. Therefore, models of stochastic cell fate decisions only determined by noisy gene expression seem inadequate to fully explain how a stochastic decision could be coordinated in a multicellular organism. However, molecular noise that alters gene expression still seems to provide an important role. One striking example, conserved in development from *Drosophila* to humans, is the stochastic choice of photoreceptor cells in the retina to cell-autonomously select to express only one photopigment from a total of three photopigments, with each stochastically picked at a defined frequency (Roorda and Williams, 1999; Smallwood et al., 2002). Using *Drosophila* as a model system, stochastic expression of a transcription factor, Spineless *(*Ss*),* was identified as the mechanism for the stochastic photopigment selection, since high levels of Ss expression correlated with the frequency of a particular fate, while cells with lower levels of Ss correlated with the alternative cell fate, indicating the cell fate choice occurs by the creation of bimodality in the level of the *spineless* expression (Wernet et al., 2006). How the bimodality arose upstream in the genetic network and what sources of noise or variability could be responsible for variable expression still remains a question.

In general, specific details about stochastic cell fate decisions have been difficult to obtain since many studies have been limited by their inability to track components over time, which is required to disentangle the relationship between molecular noise, expression dynamics, or expression levels of a particular protein and also directly observe the adoption of a

particular cell fate. To overcome this, we look at a stochastic decision in *C. elegans* where we can follow and track individual cells over time to observe the cell fate decision-making process, and examine the mechanisms and processes that allow for bimodality to develop in the genetic network.

A cell-autonomous stochastic cell fate decision in *C. elegans* involves a decision between adoption of a hypodermal fate or whether to remain a competent precursor cell (Figure 1b). The cell that faces this decision, the P3.p cell, is a member of the vulval precursor cell (VPC) competence group, a group which is defined by its ability to form the vulva. The group of six cells named, named P3.p-P8.p, are located in the ventral nerve cord of the nematode and obtain different vulval fates depending on their exposure to external signals (Eisenmann et al., 1998; Félix, 2012; Gleason et al., 2001; Gupta et al., 2012; Hill and Sternberg, 1993; Sternberg and Horvitz, 1986). During the L2 stage of nematode development, the hypodermal fate arises through a cell fusion event in which the cell becomes hypodermal by fusing to an existing neighboring hypodermal cell, the hyp7 cell (Shemer and Podbilewicz, 2002). In other animals, the cell does not fuse and remains as a VPC-fated cell, allowing us to definitively score the frequency of each particular cell fate depending on whether the cell fused or not (Fig. 1b).

Many distinct genetic signaling pathways have already been identified that regulate or alter the frequency of cell fusion fates that could be potential sources of variability that influence the outcome of the stochastic cell fate decision. The Hox genes are a conserved and essential class of developmental regulators of cell fate and developmental patterning (Koh et al., 2002; Salser et al., 1993). Mutations in the *C. elegans* Hox gene *lin-39* have been shown to impact the Pn.p cell fate frequencies due to its major role in the regulation of Pn.p cell competence, promotion of cell division, and repressor of cell fusion (Clark et al., 1993; Koh et al., 2002; Maloof and Kenyon, 1998; Roiz et al., 2016; Shemer and Podbilewicz, 2002). LIN-39 is essential for vuvlal development, since *lin-39* null mutations causes the Pn.p cells to prematurely fuse, resulting in a Vulvaless phenotype, while overexpression of LIN-39 reduces the frequency of cell fusions, suggesting that levels of LIN-39 could bias the cell-fate decision (Clark et al., 1993; Pénigault and Félix, 2011a).

In parallel to the HOX pathway, the Wnt/β-catenin signaling pathway is also required for the competence of the Pn.p cells during the L2 stage (Gleason et al., 2001; Myers and Greenwald, 2007). The Wnt pathway is a highly conserved signaling pathway that regulates many developmental events and cell fates (Hirabayashi, 2004; Hudson et al., 2013; Lindström et al., 2014; Mucenski et al., 2003; Ohyama, 2006). The pathway includes secreted exracellular Wnt ligands that are detected by Wnt receptors, allowing for signaling and communication at a distance. In general, when Wnt ligands are present, continuous degradation of the β -catenin complex is halted, allowing β –catenin to accumulate and enter the nucleus to co-regulate gene expression (Korswagen, 2002; Sawa and Korswagen, 2013). In *C. elegans*, the Wnt pathway has expanded with multiple β -catenin homologs and the BAR-1 homolog regulating the fate of the Pn.p cells (Eisenmann et al., 1998; Korswagen et al., 2000). Mutations in the Wnt ligand *cwn-1* or *bar-1* cause an increase in hyp7/fusion fate frequency. Previous investigations into the P3.p stochastic cell fate decision showed the P3.p cell extremely sensitive to the levels of Wnt

ligands, suggesting that noise or variability in the gradient or distribution of ligands could provide the variation required to cause a stochastic cell fate decision (Pénigault and Félix, 2011a, 2011b). However, the activities of individual components of the Wnt pathway in the Pn.p cells are largely unexplored, such as the dynamics or strength of signaling, which could introduce variability or noise into the system.

To investigate the components that regulate the stochastic cell fate decision, we used time-lapse microscopy and quantitative gene expression analysis to measure and identify sources of noise in the genetic network that could correlate to a specific cell fate outcome. Our goal is to seek out sources of variability that could bias or influence the cell-fate decision, such as levels of regulators or activity of certain pathways, and determine whether that variability correlated or could result in producing a stochastic outcome. Additionally, we want to identify where bimodality developed in the genetic network, and how and via what mechanisms it could be generated.

For the first time we can follow individual cells during the cell-fate decision process to directly observe and correlate gene expression and signaling activity to cell fate outcome. This approach also allowed us to also explore the temporal aspects of stochastic cell fate decisions, and we discovered they are surprisingly regulated with an apparent mechanism in place to ensure that the cell-autonomous decision is executed at the proper time of development. In addition, we characterized multiple sources of noise and identified they act with different mechanisms to introduce variability into the system. We find novel aspects of Wnt signaling only observable using time-lapse microscopy, and that the primary source of noise that also biases the cell fate decision is the timing β-catenin/BAR-1 of activation. Overall, we present a model for cell-autonomous and stochastic cell fate decisions that can be tuned and regulated without disrupting temporal aspects, an essential feature for proper development.

Materials and Methods

C*. elegans* strains and culture

All strains were handled according to the standard protocol on Nematode growth medium (NGM) agar plates with OP50 bacteria (Brenner, 1974). All strains were obtained from the CGC unless otherwise indicated. The following mutations were used in this study: LGI: *dpy-5(e907),* LGII: *cwn-1(ok546)* referred to in this paper as *cwn-1(0),* LGIII*: lin-39(n709)* referred to in this paper as *lin-39(lf)*, *unc-119(ed3),* LGIV: *unc-30(e191),* and LGX: *bar-1(ga80).* The following transgenes were used in this study: *ncIs13[ajm-1::GFP], sIs11337[rCesY37A1B.5::GFP + pCeh361)], ouIs20 [ajm-1::mCherry + unc-119+]* obtained from Alison Woollard*, itIs37 [pie-1p::mCherry::H2B::pie-1 3'UTR + unc-119(+)] IV, stIs10116 [his-72(promoter)::his-24::mCherry::let-858 3'UTR + unc-119(+)], stIs10311 [lin-39::TGF(3D3)::GFP::TY1::3xFLAG])* referred to in this paper as LIN-39::GFP*, gaIs45[pDE218(bar-1::bar-1::GFP)]* obtained from David Eisenmann and referred to in this paper as BAR-1::GFP or *bar-1(++),* (Eisenmann et al., 1998), *stIs10226[his-72p::HIS-24::mCherry::let-858 3' UTR + unc-119(+)]*. The presence of the *cwn-1(ok546)* homozygous mutation was confirmed in the created strains by nested PCR screening of candidate strains. The following primers were used for the nested PCR: outer left (’5-TCGTTTCTGACATGGCTCAC-3’), outer right (‘5-ACCCATCCTTTCCCAATCTC-3’), inner left (‘5-CGTATCCACGACCACAACAG-3’) and inner right (5’-AGAATCTTCACACCAACGGG-3’).

Time-lapse imaging

The microchamber size used in the study was 190 µm x 190 µm, with a depth of 10 µm and made as previously described and imaged with a custom time-lapse microscope (Gritti et al., 2016). Using an eyelash attached to a glass pipette, bacteria was used as “glue” to transfer eggs into the microchambers. Generally, the assembled microchamber was then allowed to sit at 19° for approximately 16 hrs before image acquisition. A Nikon Ti-E inverted microscope with a large chip camera (Hamamatsu sCMOS Orca v2) and a 60 X magnification objective (NA=1.4 oil immersion) was used. Transmission imaging was performed using an LED light source (CoolLED pE-100 615nm), while 488 nm and 561 nm fluorescence images were acquired using Coherent OBIS LS 488-100 and OBIS LS 561-100 lasers, respectively. Images were acquired in a temperature controlled room at 19° with a sample temperature of approximately 23°. Exposure time was 10 ms and approximately 25 images were taken with a z-distance of 1 µm. Images were taken every 20 min.

Image Analysis

Custom Python software was used to analyze the acquired images. Images to be used for quantitative analysis were first corrected for uneven laser illumination by a normalization procedure to correct for position-specific differences in laser intensity. For all experiments, the transmitted light images where used to identify molt times. Pn.p cells were identified by its stereotyped nuclear position location and the domains of AJM-1*::*GFP expression, if present. To

measure LIN-39::GFP expression, a mask was hand annotated around each nucleus and the mean fluorescence intensity of the pixels within the mask was calculated. A background fluorescence measurement was calculated near the P3.p and P4.p nuclei by sampling a region near the cells along the axis of the ventral nerve cord. The background measurement was then subtracted from the mean fluorescence intensity for that image to correct. To measure BAR-1::GFP expression, a mask was created around each Pn.p cytoplasmic region using *AJM-1::mCherry* signal as a positional guide. The background measurement calculation and correct was determined similarly as LIN-39::GFP.

Single-molecule fluorescence in situ hybridization (smFISH)

Probe design and smFISH hybridization to visualize *eff-1* mRNA transcripts were performed as previously described (Huelsz-Prince and van Zon, 2017; Raj et al., 2008). Custom Stellaris® FISH Probes were designed against the exons of the *eff-1* gene by utilizing the Stellaris® RNA FISH Probe Designer (Biosearch Technologies, Inc., Petaluma, CA) available online at www.biosearchtech.com/stellarisdesigner. The probes were hybridized with the Cy5 dye (Huelsz-Prince and van Zon, 2017). The sequences of the oligonucleotide probes used in this study are listed in Table 2 of the Supplementary Figures. Animals were collected by washing plates with M9 and were fixed in 4% formaldehyde in 1X PBS for 45min at room temperature. Fixed animals were permeabilized in 70% ethanol at least one night at 4°. Subsequently, animals were incubated with the 0.5 µl smFISH probes overnight at 30° in Stellaris® Hybridization Solution containing 10% formamide. The next day, animals were quickly washed two times with 10% formamide and 2 X SSC, followed by an incubation wash for 30 min at 30°. DAPI was added at 0.01 µg/ml in a final incubation step for 20 min at 30° C. Animals were mounted in Glox Buffer with catalase and glucose oxidase, and images were acquired with a Nikon Ti-E inverted fluorescence microscope, equipped with a 100 X plan-apochromat oil-immersion objective and an Andor Ikon-M CCD camera controlled by µManager software (Edelstein et al., 2014). Stacks of each animal were taken with a z-distance of 0.33 µm and approximately 30 images were taken per animal. Cy5 exposure time was 3 s, while DAPI and GFP exposure time were 100 ms and 500 ms, respectively. Animals were then imaged at 40 X to determine their body length, which was measured by drawing a spline from the tip of the worms head to the end of the tail. smFISH images were analyzed with a custom Python script using techniques previously described (Raj et al., 2008).

Modeling

Details of the models are available in Supplementary Methods.

Data Availability

Currently, data and scripts are available upon request.

Results

Time-lapse microscopy of a stochastic cell fate decision

So far, whether P3.p undergoes fusion or assumes VPC fate in wild-type or mutant animals has been assessed only after the process has completed (Alper and Kenyon, 2001, 2002; Chen and Han, 2001; Eisenmann et al., 1998; Myers and Greenwald, 2007; Pénigault and Félix, 2011a, 2011b). To correlate early stochastic molecular events to eventual cell fate outcome it is essential to follow these processes directly in time. Here, we utilize a novel fluorescent time-lapse microscopy approach that makes it possible to study single-cell dynamics inside *C. elegans* larvae for their entire ~40h development (Gritti et al., 2016) We tested whether we could directly observe P3.p fusion dynamics inside single animals. We used two independent measures of cell fusion: first, the apical junction protein AJM-1, which accumulates in Pn.p cells but is degraded upon cell fusion (Brabin et al., 2011). Second, flow of GFP from the hypodermis into the fusing cell, using animals carrying an extrachromosal array that targets GFP expression to the hyp7 hypodermal syncytium. In all animals, we saw that AJM-1::mCherry in the P3.p cell expanded along the A-P direction during the early L2 larval stage, until it made contact with AJM-1::mCherry in P4.p after ~5h (Supplementary Movies 1-2, Fig. 1c,d), as observed before (Shemer et al., 2004). This was followed by a pronounced ruffling of the AJM-1:mCherry signal and a rapid retraction of AJM-1::mCherry towards the posterior, with the fluorescence signal fully disappearing from P3.p within ~1hr (Fig. 1c,d). Inflow of GFP from the hypodermis into P3.p was observed as soon as AJM-1::mCherry retraction commenced (Fig. 1c,d,e), showing that the changes in AJM-1 were not a delayed response to but instead coincided directly with P3.p fusion. For this reason and because the AJM-1 signal could be easily monitored in parallel with other fluorescent reporters in the same channel, we used AJM-1 dynamics to establish (timing of) P3.p fusion for all subsequent experiments.

Even though changes to the frequency of P3.p Hyp7/fusion versus VPC fate in mutants are well studied (Alper and Kenyon, 2001, 2002; Chen and Han, 2001; Eisenmann et al., 1998; Myers and Greenwald, 2007; Pénigault and Félix, 2011a, 2011b), it was not known how such mutants impact the timing of this decision (Fig. 1f). We envisioned two opposing scenarios for how changes in P3.p fusion frequency could impact timing of fusion, depending on the mechanism underlying the stochastic cell fate decision. In the ‘integrator’ model, P3.p would integrate over a stochastically varying input signal, presumably Wnt signaling, by the slow stochastic accumulation of a downstream signal. Fusion would occur once the level of this signal passes a particular threshold. In such a model, mutants in which P3.p fusion frequency is increased would also exhibit fusion significantly earlier (Supplementary Fig. 1a). In contrast, in the ‘snapshot’ model, P3.p cells would make an instantaneous measurement of the stochastically varying input signal, with P3.p fusion occurring only when the input exceeds a threshold. In this scenario, changes in frequency would not affect timing of P3.p fusion (Supplementary Fig. 1b). We quantified the time of P3.p fusion in wild-type animals, carrying only the AJM-1::GFP reporter, and found that cell fusion occurred in a relatively narrow time window at 40-60% of the L2 larval stage (Fig. 1g). We then examined *bar-1(ga80)*, *cwn-*

1(ok546) and *lin-39(n709)* mutants, in which P3.p fusion frequency is significantly increased (Fig. 1f,g). We found that in these mutants P3.p fusion occurred within the same time window as wild-type animals, with only small differences between wild-type and mutant animals in average timing (Supplementary Fig. 1c). In these mutants often additional Pn.p cells, such as P4.p, assume hypodermal fate and fuse (Fig. 1f,g). Strikingly, even though the exact time of fusion can vary as much as 2h between animals, when multiple VPCs fuse in a single animal, they typically do so at the same time (Fig. 1h). This is strong evidence that the stochastic decision between hypodermal and VPC fate is triggered by a global signal that impacts multiple Pn.p cells simultaneously. In general, these results show that cell fate frequency is regulated independently of its exact timing, favoring a 'snapshot' model as its control mechanism. How such a model might be implemented on the molecular level is discussed further below.

Bimodal *eff-1* expression precedes P3.p fusion

It is generally assumed that stochastic cell fate decisions are preceded by bimodal expression of cell date determinants (Fig. 1a) (Gamba et al., 2015; Wernet et al., 2006). Currently, it is not known if and where in the signaling network that controls the Hyp7/fusion versus VPC fate decision such a bimodal distribution arises. To examine this, we used single-molecule FISH (smFISH) to characterize the expression of the downstream-most effector of P3.p fusion, the fusogen *eff-1* that is necessary and sufficient to cause cell fusion (Mohler et al., 2002; Shemer et al., 2004). EFF-1 is a transmembrane protein that is required for most epithelial cell fusions in *C. elegans*, and is required on the plasma membrane of both cells that will fuse, in this case, the Pn.p cell and the hyp7 plasma membrane (Zeev-Ben-Mordehai et al. 2014; Smurova and Podbilewicz 2016;). We wanted to differentiate between two hypotheses: first, that *eff-1* is expressed in a bimodal manner, with low *eff-1* mRNA levels in P3.p cells that assume VPC fate, but high *eff-1* mRNA levels just prior to fusion in P3.p cells that assume Hyp7/fusion fate. Alternatively, that *eff-1* expression exhibits a broad, continuous distribution, with only those cells where *eff-1* levels rise above a threshold value fusing. In AJM-1::GFP animals we quantified *eff-1* mRNA levels in animals where P3.p had not undergone fusion, based on presence and unruffled appearance of the AJM-1 signal (Fig. 2a,b). As animals were fixed for the smFISH protocol, they consisted of two classes between which we could not distinguish: those where P3.p would have assumed VPC fate and never fused and those where P3.p would have assumed hyp7/fusion fate but had not yet fused. Consistently, we found that in most animals *eff-1* mRNA was present in P3.p at low levels, <10 molecules, similar to the level observed in P4.p, which never fuses (Fig. 2c,d). However, in the range of body lengths (340-380 μm) corresponding to the measured time of fusion, we observed that a subset of animals expressed *eff-1* at high levels, 30-50 molecules (Fig. 2c,d). Interestingly, similar high levels were seen at the same time in P2.p cells, even though they have already fused to the hyp7 syncytium one larval stage earlier. In addition, we observed that *eff-1* expression remained high in recently fused P3.p cells, as judged on the ruffling or absence of AJM-1, before disappearing by the end of the L2 stage (Supplementary Fig. 2a). To confirm that high *eff-1* expression preceded cell fusion and was not induced by any cell fusion events that happen to rapid to be captured by changes in AJM-1 localization, we examined *eff-1* expression in mutants with a temperature-sensitive loss-of-function point mutation in *eff-1* (Mohler et al., 2002). Indeed, at the restrictive

temperature we still found high levels of *eff-1* mRNA in P3.p, but not P4.p, even as P3.p cell fusion was fully inhibited (Supplemental Fig. 2b).

Although the resulting *eff-1* distribution is bimodal (Fig. 2d), the fraction of P3.p cells expressing high *eff-1* levels was smaller than the observed frequency of cell fusion in this strain (Fig. 1f), indicating that *eff-1* was expressed at high levels for only a short duration before the cell fuses. If bimodal *eff-1* expression is the driver of the stochastic Hyp7/fusion versus VPC fate decision, then in mutants where the cell fate frequency is different the height of the two peaks rather than the overall width of *eff-1* distribution would be changed (Fig. 1a). To test this prediction we quantified *eff-1* levels in two mutants with changed P3.p fusion frequency. First, we used a mutant carrying a functional LIN-39::GFP insertion, an inhibitor of P3.p fusion (Fig. 1b), which has low (~2%) P3.p fusion frequency. Indeed we found that here the *eff-1* distribution only showed a peak at low *eff-1* levels (Fig. 2e). In contrast, in a *cwn-1(ok546)* mutant with high (>90%) P3.p fusion, the peak at low *eff-1* was much reduced and instead more animals showed high *eff-1* expression (Fig. 2f), even though the absolute *eff-1* level in these animals was not significantly elevated compared to animals with wild-type fusion frequency (Fig. 2d).

Taken together, these results show that *eff-1* expression is bimodal at the time of the hyp7/fusion versus VPC fate decision, with the amplitude of both peaks in the distribution changing in accordance with the frequency of P3.p hyp7/fusion fate in mutants. This raises the question how bimodal *eff-1* expression is generated and controlled by the upstream signaling network (Fig. 1b). One possibility is that the activity of upstream signaling proteins is already bimodal. Alternatively, the activity of the actors just upstream of *eff-1* might be stochastic but in a graded, continuous manner and bimodality in *eff-1* might generated by interactions between these different layers of the signaling network. To address this question, we next examined variability in known upstream regulators of *eff-1* expression.

Bias of cell fate decision by noise in LIN-39 protein level

The Hox transcription factor LIN-39 inhibits Pn.p hyp7/fusion fate by repressing *eff-1* expression (Shemer and Podbilewicz, 2002), with *lin-39* null mutations causing all Pn.p cells to fuse in the L1 larval stage (Clark et al., 1993; Wang et al., 1993). Hence, stochastic variability in LIN-39 protein levels could be a driver of bimodal *eff-1* expression, with *eff-1* upregulated only in P3.p cells where LIN-39 levels falls below a threshold. It was shown previously that LIN-39 levels are similar between P3.p and P4.p in early L2 larval stage animals prior to cell fusion (Pénigault and Félix, 2011a), even though both cells have strikingly different frequency of Hyp7/fusion versus VPC fate (Fig. 1f). This indicates that absolute LIN-39 levels are unlikely to explain the difference in cell fate bias between P3.p and P4.p. However, it is possible that the dependence of *eff-1* expression on LIN-39 level differs between P3.p and P4.p and that variability in LIN-39 levels in P3.p between animals is indeed sufficient to explain the outcome of the P3.p cell fate decision. To connect animal-to-animal variability in LIN-39 level with P3.p cell fate, it is essential to monitor LIN-39 dynamics and cell fusion in time in single animals. To achieve this, we performed time-lapse microscopy on animals carrying a LIN-39::GFP translational fusion (Sarov et al., 2014) and AJM-1::GFP as a cell fusion marker

(Supplementary Movies 3-4, Fig. 3a,b). Since LIN-39::GFP is present as a multi-copy insertion, it decreased the P3.p fusion rate from ~30% to ~2%, making it challenging to capture sufficient P3.p fusion events. For that reason, we further crossed these reporters into a *cwn-1(ok546)* background that lacks a Wnt ligand, elevating P3.p and P4.p fusion rate to 12% and 7%, respectively (Supplementary Table 1).

We observed that LIN-39 was present in the P3.p nucleus at the start of the L2 larval stage and remained there for the entire larval stage when P3.p assumed VPC fate (Fig. 3a). However, in P3.p cells that fused, nuclear LIN-39 levels decreased rapidly as soon as fusion commenced and fully disappeared within 90 mins (Fig.3b), consistent with observations in Ref. (Pénigault and Félix, 2011a). We quantified nuclear LIN-39 dynamics in P3.p in multiple animals (Fig. 3c). On average, LIN-39 levels fell during the early L2 larval stage, reaching a minimum around the time of P3.p fusion even in non-fusing P3.p cells. However, we observed significant variability in LIN-39 levels, both in time and between different animals. To test whether this variability correlated with P3.p cell fate outcome, we compared the distribution of LIN-39 levels, averaged over 6 hrs prior to fusion in P3.p cells, that assumed hyp7/fusion fate with the distribution in P3.p cells that assumed VPC fate for the same time window but now prior to the average time of P3.p fusion measured for this strain (Fig. 3d). We find a strong overlap between the two distributions, even if we increase the time window (Supplementary Fig. 3a) making it unlikely that variability in absolute LIN-39 level is the sole noise source driving bimodal *eff-1* expression and the decision to fuse. These observations were performed in a mutant lacking the Wnt ligand *cwn-1*, but this change in Wnt levels did not impact LIN-39 levels, as LIN-39 dynamics and levels were quantitatively similar in the small number of animals that undergo P3.p fusion with wild-type Wnt levels (data not shown and consistent with Ref. (Pénigault and Félix, 2011a)).

These results leave open the question whether the observed variability in LIN-39 has any effect on the P3.p cell fate outcome. LIN-39 inhibits *eff-1* expression in parallel with the Wnt signaling pathway (Fig. 1b) and variability in Wnt signaling could instead be the main driver of the P3.p cell fate decision. A mathematical model of this network (Fig. 3e) showed that both when variability in Wnt was the sole driver of the cell fate decision and when variability in Wnt and LIN-39 contributed in equal measure, the distribution of LIN-39 levels between cells that do not fuse and those that do, overlapped substantially (Fig. 3f), similar to our data (Fig. 3d). However, the model predicted that we could differentiate between these two scenarios, by comparing the difference in LIN-39 levels between pairs of cells, where one fuses and one does not: if noise in LIN-39 and Wnt drive the stochastic decision with similar strengths, fusing cells will have lower LIN-39 levels than non-fusing cells, even when based on absolute LIN-39 levels we cannot predict which cell will fuse (Fig. 3g). If only noise in Wnt signaling drives the stochastic decision, then difference in LIN-39 levels will not be predictive of cell fate when comparing pairs of cells (Fig. 3g).

In LIN-39::GFP*; cwn-1(ok546)* animals, not only P3.p but also P4.p assumed hyp7/fusion fate in a stochastic manner, (Supplementary Table 1), allowing us to test whether differences in LIN-39 levels between P3.p and P4.p are correlated with their eventual fate. First,

we established that in this strain LIN-39 distributions for P3.p and P4.p were similar and also in P4.p showed substantial overlap between fusing and non-fusing cells (Supplementary Fig. 3b). We then selected animals in which one cell, either P3.p or P4.p, fused but the other assumed VPC fate (Fig. 3h). Indeed, in these animals absolute LIN-39 level was not predictive of the eventual fate of P3.p or P4.p, but we observed a significant correlation between fate and the difference in LIN-39 levels between P3.p and P4.p (Fig. 3i), with fusing cells having lower LIN-39 than their non-fusing neighbor cell. This shows that noise in LIN-39 levels drives the hyp7/fusion versus VPC fate decision, but likely in conjunction with another noise source.

β-catenin activation dynamics during the cell fate decision

To test whether the noise source acting in parallel to noise in LIN-39 levels is found within the Wnt signaling pathway, we quantified activation of the Wnt pathway by monitoring the accumulation dynamics of BAR-1/β-catenin during the stochastic decision, in a strain carrying a functional BAR-1::GFP reporter (Eisenmann et al., 1998). Upon activation by Wnt ligands, the continual degradation of β-catenin stops and the protein accumulates in the cell and nucleus (Sawa and Korswagen, 2013). In P3.p, the presence of BAR-1 is required to inhibit hyp7/fusion fate and *eff-1* expression, in parallel to LIN-39 (Eisenmann et al., 1998). In contrast to β-catenins involved in the Wnt asymmetry pathway (Mila et al., 2015; Park and Priess, 2003), dynamics of BAR-1 during canonical Wnt signaling is poorly characterized. Based on previous observations (Eisenmann et al., 1998), we expected BAR-1 to show approximately constant levels in P(3-8).p cells, similar to LIN-39. Instead, we found that BAR-1::GFP levels were strikingly dynamic, with no BAR-1::GFP in P(3-8).p at the start of the L2 stage - though some non-Pn.p cells were expressing GFP at this time - followed by strong, coordinated pulse of BAR-1::GFP accumulation in P(3-8).p at the mid-L2 stage that lasted 1-4 hours (Supplementary Movie 5, Fig. 4a-c). The BAR-1::GFP signal was detected both in the nucleus and cytoplasm. Additionally, the P3.p cell, which is thought to be the farthest from the source of Wnt ligands (Harterink et al., 2011; Pénigault and Félix, 2011b), did not always exhibit the lowest BAR-1::GFP levels (Fig. 4c), suggesting that cell-intrinsic factors influence the degree of β-catenin activation in each Pn.p cell. Interestingly, the amplitude of the BAR-1::GFP pulse was variable both between cells (Fig. 4b,c) and when comparing the same cell between different animals (Fig. 4d), as was the time at which BAR-1::GFP began accumulating (Fig. 4d).

In BAR-1::GFP reporter animals, no P(3-8).p cells fused during the L2 stage in 30 animals (Supplementary Table 1), indicating that the fluorescently tagged BAR-1 is functional and gives rise to a BAR-1 overexpression phenotype. To reflect this, we will refer to the BAR-1 reporter strain as *bar-1(++)*. To increase the frequency of hyp7/fusion fate, we used two different approaches. First, we removed the inhibitor LIN-39, using the *lin-39(n709)* temperature sensitive loss-of-function mutant to bypass the requirement for *lin-39* during the L1 larval stage, leading to 16/70 P3.p cells assuming hyp7/fusion fate in *bar-1(++);lin-39(lf)* animals (Supplementary table 1). We found that *bar-1(++);lin39(lf)* animals showed similar BAR-1::GFP pulses, although with reduced amplitude (Fig. 4e), suggesting that LIN-39 influences Wnt signaling upstream of BAR-1. Next, we sought to lower BAR-1 levels in the *bar-1(++)* background by decreasing activity of the Wnt signaling pathway, using a *cwn-1(ok546)* loss-of-

function mutation that lacks the Wnt ligand *cwn-1*. As expected, in these animals 4/59 P3.p cells assumed hyp7/fusion fate (Supplementary Table 1) and BAR-1::GFP levels were reduced (Fig. 4f). However, we found that in *bar-1(++);cwn-1(0)* animals, BAR-1::GFP pulses were significantly delayed and occurred later in the larval stage when compared to *bar-1(++)* and *bar-1(++);lin-39(lf)* animals.

Variability in β-catenin pulse dynamics

To characterize variability in BAR-1 accumulation dynamics, we used a simple mathematical model of BAR-1 dynamics to fit to the experimental data (Fig. 5a, see Materials and Methods for details). Briefly, we assume that prior to the BAR-1 pulse, Wnt signaling is inactivated and BAR-1 is degraded. At time t_0, Wnt signaling is activated, leading to inhibition of BAR-1 degradation and hence linear accumulation of BAR-1 in the cell. Linear BAR-1 accumulation continues for a pulse duration T in cells that assume VPC fate or until the time of fusion, t_{fusion}, in cells that assume hyp7/fusion fate. Upon fusion BAR-1 vanishes immediately, whereas in cells that assume VPC fate, BAR-1 levels decrease exponentially once the pulse ends. This simple model fitted the experimental data surprisingly well (Fig. 5a,b). Moreover, it allowed us to describe each BAR-1 pulse by three parameters: pulse onset time t_0, pulse slope s and pulse duration T for VPC cells or fusion time t_{fusion} for hyp7/fusion cells.

We first compared the timing of the onset of BAR-1 accumulation between P3.p and P4.p cells. Both in *bar-1(++)* and *bar-1(++);lin-39(lf)* animals, considerable variability existed in t_0, the time of the onset of the BAR-1 pulse, between these cells, with BAR-1 accumulation in P3.p preceding that in P4.p as often as the reverse (Fig. 5b,c). At the same time, pulse onset was correlated between P3.p and P4.p, meaning that if BAR-1 accumulation started late in the L2 larval stage in P3.p, it was also likely to start late in P4.p (Fig. 5c). Strikingly, we not only found that in the *bar-1(++); cwn-1(0)* mutant the onset of the BAR-1 pulse was delayed, but also that the variability in pulse onset time between P3.p and P4.p was much reduced, with the onset of BAR-1 accumulation occurring in P3.p and P4.p within 20 mins in all animals (Fig. 5c). This result suggests that the Wnt ligand *cwn-1* not only controls the average onset of BAR-1 pulses, but also induces variability in onset time between P3.p and P4.p.

We also observed a clear variability in the duration of BAR-1 pulses when comparing pulses in the same cell between animals (Fig. 5b,d). We examined whether the onset and the duration of BAR-1 pulses were correlated. Because the duration of the L2 larval stage varied both between strains and between animals in the same strain, we examined the pulse onset time t_0/T_{L2} and duration T/T_{L2} relative to the duration of the larval stage, T_{L2}. In this case, we found a striking anti-correlation, with late pulse onset resulting in shorter pulses (Fig. 5d). In fact, the data for all strains clustered along the line $T/T_{\mathrm{L2}} = 0.66 - t_0/T_{\mathrm{L2}}$, consistent with a model in which the end of the BAR-1 accumulation occurs at 66% of the L2 larval stage independent of the BAR-1 pulse onset time. Strikingly, this correlation also held for the *bar-1(++); cwn-1(0)* mutant, where not only the onset of BAR-1 pulses was delayed but also the L2 larval stage was much extended , lasting up to 22 hrs compared to ~12 hrs for wild-type animals). This also

means that Wnt signaling, in contrast to the pulse onset, likely plays no role in determining the end of the pulse.

Giving the observed qualitative difference in the degree of variability of the start and the end time of BAR-1 pulses, we next asked whether the time of fusion correlated most strongly with the start or the end of the pulse. In the first case, it would mean that the time of fusion would show strong variability with respect to both the start of the L2 larval stage and the end of the pulse, whereas in the latter case it would mean that fusion would occur at a fixed fraction of the larval stage duration. We tested this in *bar-1(++);lin-39(lf)* animals, where the largest fraction of Pn.p cells, typically P3.p, assume hyp7/fusion fate. However, because the amplitude of the BAR-1 pulses in P3.p is often low (Fig. 4e), making it challenging to accurately determine the pulse onset time t_0, we compared within the same animal the fusion time t_{fusion} in P3.p cells that assume hyp7/fusion fate with either the pulse onset time t_0 or pulse end time $t_0 + T$ in P4.p cells that assume VPC fate (Fig. 4a,e, Supplementary Fig. 5a). Strikingly, we find that the time of fusion is more strongly correlated with the pulse onset time (R=0.86) than with the pulse end time. In particular, the data clustered tightly along the line $t_{\mathrm{fusion}}/T_{\mathrm{L2}} = 0.2 + t_0/T_{\mathrm{L2}}$, suggesting that cell fusion occurs at a time $0.2T_{\mathrm{L2}}$, or on average ~2 hrs, after the onset of the BAR-1 pulse. Together, these results suggest a model in which the timing of pulse onset and cell fusion are co-regulated, independently of timing of the BAR-1 pulse end and in a manner that is highly variable between animals.

Finally, we compared the distribution of the onset time t_0 and linear slope s of BAR-1 accumulation pulses between strains. We found that not only t_0 but also pulse slope s were highly variable between animals in all strains (Fig. 5f,g). We found that the pulse parameters of *bar-1(++)* and *bar-1(++);lin-39(lf)* were similar, although we did observe more pulses with low slope in *bar-1(++);lin-39(lf)*, consistent with the assumption that difference in hyp7/fusion fate frequency is largely due to absence of the fusion inhibitor LIN-39. We assumed that the increase in frequency of hyp7/fusion fate in *bar-1(++);cwn-1(0)* animals was due to a decrease in BAR-1 level. In the context of the observed BAR-1 pulses this could be achieved in two independent ways, either by decreasing the slope s or by delaying the onset time t_0 of the BAR-1 pulse (Fig. 6a,b). Given that BAR-1 accumulation is thought to be proportional to the amount of external Wnt ligands, we expected the *cwn-1(0)* mutant to predominantly lead to a decrease in the rate of BAR-1 accumulation. Surprisingly, we found that the pulse slope distribution was highly similar for *bar-1(++)* and *bar-1(++);cwn-1(0)* animals (Fig. 5f) and that the only different pulse characteristic was the delayed pulse onset (Fig. 5g).

Bias of cell fate decision by variability in β-catenin pulse timing

To understand how variability in BAR-1 pulse dynamics influences hyp7/fusion versus VPC fate decision, we extended our mathematical model of the cell fate induction network to include BAR-1 pulses (Fig. 6a). Specifically, we assumed that at time t_0 the level of inhibition by Wnt signaling, $c_w(t)$, increases with linear slope s, with stochastic variability in both variables. Currently, factors that induce *eff-1* expression or hyp7/fusion fate are not known. However, our observations suggest that induction of hyp7/fusion cell fate must also be under temporal control.

First, cell fusion does not occur at the start of the L2 larval stage, even though the inhibitor BAR-1 is not present (Fig. 5a). Moreover, the time of fusion is itself variable but correlated with the start of the BAR-1 pulse (Fig. 5e). In the model, we therefore assume that a signal to activate *eff-1* expression is present from time t_{fusion} with level c_a, again with stochastic variability in both variables. Fusion occurs when at time t_{fusion} the inhibitory Wnt signal c_w is sufficiently low that the *eff-1* level $e(t)$ is above the threshold e_{th} required to induce fusion. In the model, this can be achieved both by stochastic variability in pulse slope and pulse onset timing (Fig. 6b). In general, this extended model reproduces the experimentally observed characteristic of BAR-1 pulse timing (Supplementary Fig. 6a).

The model can explain the increased frequency of hyp7/fusion in *bar-1(++); lin-39(lf)* and *bar-1(++); cwn-1(0)* animals. First, the decrease of *eff-1* inhibition by the absence of LIN-39 in the *lin-39(lf)* background increases the range of activating and inhibitory signals c_a and c_w for which *eff-1* is expressed above the threshold e_{th}, so that a higher fraction of the animals with elevated BAR-1 levels in the *bar-1(++)* background still result in fusion (Fig. 6c). In contrast, for the *bar-1(++); cwn-1(0)* mutant, the observed delay in pulse onset causes lower inhibitory Wnt signals c_w at the time of fusion, leading to more frequent fusion events. Specifically, in many animals the onset of the BAR-1 pulse occurs after expression of *eff-1* is induced by the activator, i.e. c_w=0 at the time of fusion.

Next, we used experimentally testable predictions to establish the relative importance of variability in BAR-1 pulse timing and pulse slope in biasing the hyp7/fusion versus VPC fate decision. First, the model predicted that when compared at the time when cell fusion is activated, BAR-1 levels in cells that assume hyp7/fusion fate should be lower than in cells that assume VPC fate (Supplementary Fig 6b). However, because we cannot infer the time of activation of cell fusion in cells that do not fuse but instead assume VPC fate, we could not test this experimentally. However, the model predicted that, if variability in pulse timing was more important for determining BAR-1 levels than variability in pulse slope, cells that fuse cannot be distinguished from those that assume VPC fate based on BAR-1 pulse slope (Fig. 6d), but that fusing cells do have a delayed pulse onset time t_0 compared to non-fusing cells (Fig. 6f). In contrast, when variability in pulse slope dominates BAR-1 levels, then fusing and non-fusing cells differ in slope rather than pulse onset time (Supplementary Fig. 6c). To test this prediction, we first compared pulse slope and pulse onset time between P3.p and P.4p cells in *bar-1(++)* animals, where these cells never assume hyp7/fusion fate. We found that the distributions $P(s_{\mathrm{P4.p}}\text{-}s_{\mathrm{P3.p}})$, of difference in pulse slope, and $P(t_{0,\mathrm{P4.p}}\text{-}t_{0,\mathrm{P3.p}})$, of difference in pulse onset time, were symmetrical, i.e. showed no systematic difference between P3.p and P4.p (Fig. 6e,g). We then examined the difference in pulse slope and onset time in *bar-1(++); lin-39(lf)* animals, comparing animals where P3.p fused but P4.p assumed VPC fate with animals where both P3.p and P4.p assumed VPC fate. We found no bias towards lower pulse slope in fusing P3.p cells compared to non-fusing P4.p cells (Fig. 6e, blue line), but instead found a distribution very similar to that observed in *bar-1(++)* animals. However, we found that BAR-1 pulse onset in fusing P3.p cells was delayed compared to non-fusing P4.p cells (Fig 6g, blue line), with only one animal with a fusing P3.p cell showing BAR-1 accumulation in P3.p prior to P4.p. This difference was particularly striking compared to the *bar-1(++)* strain, which otherwise showed no

difference in relative timing of BAR-1 pulse onset between P3.p and P4.p relative to *bar-1(++);lin-39(ts)* animals (Fig. 5c).

Even though the above results indicated that BAR-1 pulse timing biased the hyp7/fusion versus VPC fate decision, it left open whether variations in pulse timing achieve this by specifically modulating BAR-1 levels at the time the decision to fuse or not is made. We previously found that the only difference in BAR-1 pulse dynamics between *bar-1(++)* and *bar-1(++);cwn-1(0)* animals was the delayed onset of BAR-1 pulses (Fig. 5g), additional evidence that pulse timing affects cell fate frequency. Indeed, the model showed the delayed onset of BAR-1 pulses increased the frequency of hyp7/fusion fate by lowering BAR-1 levels at the time when *eff-1* expression and cell fusion is activated (Fig. 6a,b). Moreover, the model predicted that fusing cells in *bar-1(++);cwn-1(0)* mutants should have lower BAR-1 levels than fusing cells in *bar-1(++);lin-39(ts)* mutants, where fusion frequency is instead increased by removing the inhibitor LIN-39 (Fig. 6h). Indeed, when we compared BAR-1::GFP fluorescence at the time of cell fusion in *bar-1(++);lin-39(ts)* and *bar-1(++);cwn-1(0)* animals, we found a bias towards lower BAR-1 levels in fusing P3.p and P4.p cells in the *cwn-1(0)* background. This provides further evidence that delayed BAR-1 pulse timing influences the cell fate decision by reducing the inhibitory BAR-1 levels at the time the decision is made. To further link BAR-1 levels to inhibition of cell fusion, we quantified *eff-1* transcripts in *bar-1::gfp* animals and indeed found a negative correlation: Pn.p cells with visible BAR-1::GFP had few *eff-1* transcripts, while some unfused Pn.p cells without visible BAR-1::GFP showed high *eff-1* levels (Supplemental Figure 6d). Together, these results show that variability in the timing of BAR-1 accumulation pulses are a key noise source biasing the hyp7/fusion versus VPC fate decision.

Discussion

Here we describe a cell-autonomous stochastic cell fate decision using time-lapse microscopy and modeling of components of the cell-fate decision network. The bimodality we expected to find in the genetic network of a stochastic cell fate decision was at the level of *eff-1* transcription, the most downstream protein in the network and sufficient to initiate the hyp7/fusion fate. We then characterized two potential noise sources upstream of *eff-1* expression that biased the stochastic cell fate decision. Each noise source biases the cell fate decision via a different mechanism: first, variability in the relative levels of Hox/LIN-39, and second, variability in the timing of the pulse of BAR-1/β-catenin in response to Wnt ligands. Combinations between the activities of these two inhibitors created a distribution of inhibitory variability that we propose is opposed with the activity of a presumed positive regulator of *eff-1.*

To observe the localization and protein levels of LIN-39 and BAR-1, we expressed extragenic copies of proteins fused with a fluorescent markers. For both proteins, this also was associated with an overexpression phenotype, since additional copies of the protein changed the rate of P3.p cell fusions. This reduction in the P3.p fusion rate prevented the analysis or observation of hyp7/fusion fated cells in an otherwise normal genetic background. To circumvent this problem, we sensitized the genetic background using Wnt or *lin-39* mutations. With these changes, we were far from normal gene expression levels in wild-type *C. elegans*, but could exploit the situation in order to determine the principles of the stochastic decision. Interestingly, whether the P3.p cell obtains the hyp7/fusion fate or the VPC fate is actually inconsequential to the actual final developmental form of the animal (except in extreme circumstances in which other Pn.p cells are ablated), since normally the adult vulva is formed only from the P5.p, P6.p, and P7.p cells. In non-fusing P3.p cells, the cell divides once and then fuses the hypodermis at a later stage (Félix, 2012; Sternberg, 2005; Sternberg and Horvitz, 1986).

The Wnt/β-catenin pathway has been intensively studied in *C. elegans*, with a significant focus on Wnt-guided cell migration and the SYS-1/POP-1 Wnt asymmetry pathway, required for proper fate of seam cells and some neurons, while the role of BAR-1 in the Pn.p cells has remained less characterized (Eisenmann et al., 1998; Gleason et al., 2002; Harterink et al., 2011; Korswagen, 2002; Lin et al., 1998; Maloof et al., 1999; Mentink et al., 2014; Mila et al., 2015; Park and Priess, 2003; Shetty et al., 2005; Whangbo and Kenyon, 1999). While genetic evidence shows that β-catenin/BAR-1 is an inhibitor of the *eff-1* gene, it is conventionally known to act as a transcriptional co-activator with the TCF/POP-1 protein, suggesting that the effect BAR-1 has on *eff-1* is through another intermediate protein. Some descriptions of the BAR-1/β-catenin pathway have attempted to identify the changes or molecular targets of BAR-1 using RNA-sequencing in a *bar-1* mutant (Natarajan and Eisenmann, 2002). However, the specific changes in the Pn.p cells that would be relevant to the stochastic cell fate decision would be difficult to detect in bulk tissue experiments of whole animals. We found that the Wnt pathway showed interesting temporal dynamics and regulation that has not been characterized before. The temporal signaling in the Pn.p was highly cell and stage specific. Surprisingly, we found a

potentially novel aspect of Wnt pathway regulation that was only apparent from time-lapse imaging, that not only do the Pn.p cells “read out” the levels or presence of Wnts at a highly coordinated and specific time window, they also respond to the Wnt level by altering the timing of the BAR-1/β-catenin pulse, rather than the slope or accumulation rate.

The regulation of the timing of cellular and developmental events has not been widely studied in *C. elegans,* except through the heterochronic mutants, that completely lack or repeat larval stages and their associated developmental events, and through oscillating genes, such as the circadian rhythm homolog *Period/lin-42,* that are tied to the regulation of the molting pattern (Ambros and Horvitz, 1984; Hendriks et al., 2014; Moss, 2007). We found that the timing of the cell fusion event was surprisingly regulated and conserved, even in mutants that had high cell fusion frequencies, in which we naively expected the cell fusion event to have occurred much earlier. Additionally, the time length of the L2 stage in *cwn-1* mutants was especially extended compared to wild-type animals. Despite this, the timing of cell fusions occurred at a specific fraction of the way through development, suggesting that instead of development proceeding from an absolute timer that resets during each larval stage or starts from hatching, worms develop can develop with different speeds of an internal clock, with the progression of developmental events following that internal clock.

Since the distributions of characteristics between hyp7/fusion fated-cells and VPC fated cells had overlapping portions, other sources of noise and variability must also play a role in the decision. While we have mainly studied components of the inhibitory side of the genetic network, it is still unclear what transcription factor(s) are primarily responsible for the activation of *eff-1*. Most mutations that alter the frequency of the P3.p hyp7/fusion cell fate lie in proteins that act as inhibitors to the cell fusion process, such as most Wnt pathway components, *ceh-20, ref-1, ref-2, egl-18/elt-5, dyamin-1,*and *rab-5* (Alper and Kenyon, 2001, 2002; Gorrepati et al., 2013; Koh et al., 2002; Smurova and Podbilewicz, 2016). Fewer have been found that are required for *eff-1* activation, which could also provide additional noise or variability into the cell fate decision. Studies have shown a *lin-22* loss-of-function mutation decreases P3.p cell fusion frequencies (Katsanos et al., 2017; Schlager et al., 2006). LIN-22 codes for a Hairy/Enhancer of Split-related transcription factor, which was found to act in the Wnt pathway by repressing *egl-18*, a GATA transcription factor, also a repressor of cell fusion in the seam cells (Gorrepati et al., 2013; Katsanos et al., 2017; Wrischnik and Kenyon, 1997). Therefore, variations in not only the inhibitor molecules, but LIN-22 could create noise and variability that leads to stochastic *eff-1* expression and cell fusion. Additionally, the classB *synMuv* gene class has also shown to decrease cell fusion frequencies, such as mutations in *lin-35*, *efl-1*, and *hda-1*, a histone deacetylase (Chen and Han, 2001). These proteins may be more generic modifiers of transcription and influence the whole genome, and therefore don’t play a direct role in the stochastic fate decision, but the chromatin state or accessibility of the *eff-1* gene cannot be discounted.

In summary, we propose that the balance of inhibitors and activators at a critical time point is integrated into the promotor of the eff-1, which then either triggers expression or keeps the gene inactive. Cooperativity in the region of the *eff-1* promotor would then be needed to induce gene expression. In this model, the relative frequency of VPC or hypodermal fate is determined by the balance between the degree of activation relative to inhibition by BAR-1 and LIN-39.

Acknowledgements

This work is part of the research program of the Netherlands Organisation for Scientific Research (NWO) and was performed at the research institute AMOLF. Some *C. elegans* strains were provided by the CGC, which is funded by NIH Office of Research Infrastructure Programs (P40 OD010440). The work was supported by a European Research Council Starting Grant (338200-STOCHCELLFATE) awarded to J.S.v.Z.

References

Alper, S., and Kenyon, C. (2001). REF-1, a protein with two bHLH domains, alters the pattern of cell fusion in C. elegans by regulating Hox protein activity. Development *128*, 1793–1804.

Alper, S., and Kenyon, C. (2002). The zinc finger protein REF-2 functions with the Hox genes to inhibit cell fusion in the ventral epidermis of C. elegans. Development *129*, 3335–3348.

Ambros, V., and Horvitz, H. (1984). Heterochronic mutants of the nematode Caenorhabditis elegans. Science (80-.). *226*, 409–416.

Balaban, N.Q. (2004). Bacterial Persistence as a Phenotypic Switch. Science (80-.). *305*, 1622–1625.

Brabin, C., Appleford, P.J., and Woollard, A. (2011). The Caenorhabditis elegans GATA Factor ELT-1 Works through the Cell Proliferation Regulator BRO-1 and the Fusogen EFF-1 to Maintain the Seam Stem-Like Fate. PLoS Genet. *7*, e1002200.

Brenner, S. (1974). THE GENETICS OF CAENORHABDITIS ELEGANS. Genetics *77*, 71–94.

Chen, Z., and Han, M. (2001). C. elegans Rb NuRD and Ras regulate lin-39-mediated cell fusion during vulval fate specification. Curr. Biol. *11*, 1874–1879.

Clark, S.G., Chisholm, A.D., and Horvitz, H.R. (1993). Control of Cell Fates in the Central Body Region of C-Elegans By the Homeobox Gene Lin-39. Cell *74*, 43–55.

Edelstein, A.D., Tsuchida, M.A., Amodaj, N., Pinkard, H., Vale, R.D., and Stuurman, N. (2014). Advanced methods of microscope control using μManager software. J. Biol. Methods *1*, 10.

Eisenmann, D.M., Maloof, J.N., Simske, J.S., Kenyon, C., and Kim, S.K. (1998). The beta-catenin homolog BAR-1 and LET-60 Ras coordinately regulate the Hox gene lin-39 during Caenorhabditis elegans vulval development. Development *125*, 3667–3680.

Elowitz, M.B., Levine, A.J., Siggia, E.D., and Swain, P.S. (2002). Stochastic gene expression in a single cell. Science (80-.). *297*, 1183–1186.

Félix, M.A. (2012). Caenorhabditis elegans vulval cell fate patterning. Phys. Biol. *9*.

Gamba, P., Jonker, M.J., and Hamoen, L.W. (2015). A Novel Feedback Loop That Controls Bimodal Expression of Genetic Competence. PLoS Genet. *11*, 1–32.

Gleason, J., Korswagen, H.C., and Eisenmann, D.M. (2001). Activation of Wnt signaling bypasses the requirement for Ras signaling during vulval induction. Int. C. Elegans Meet. 1281–1290.

Gleason, J.E., Korswagen, H.C., and Eisenmann, D.M. (2002). Activation of Wnt signaling bypasses the requirement for RTK/Ras signaling during C. elegans vulval induction. Genes Dev. *16*, 1281–1290.

Gorrepati, L., Thompson, K.W., and Eisenmann, D.M. (2013). C. elegans GATA factors EGL-18 and ELT-6 function downstream of Wnt signaling to maintain the progenitor fate during larval asymmetric divisions of the seam cells. Development *140*, 2093–2102.

Gritti, N., Kienle, S., Filina, O., and van Zon, J.S. (2016). Long-term time-lapse microscopy of C. elegans post-embryonic development. Nat. Commun. *7*, 12500.

Gupta, B.P., Hanna-Rose, W., and Sternberg, P.W. (2012). Morphogenesis of the vulva and the vulval-uterine connection*. WormBook 1–17.

Harterink, M., Kim, D.H., Middelkoop, T.C., Doan, T.D., van Oudenaarden, A., and Korswagen, H.C. (2011). Neuroblast migration along the anteroposterior axis of C. elegans is controlled by opposing gradients of Wnts and a secreted Frizzled-related protein. Development *138*, 2915–2924.

Hendriks, G.J., Gaidatzis, D., Aeschimann, F., and Großhans, H. (2014). Extensive Oscillatory Gene Expression during C.elegans Larval Development. Mol. Cell *53*, 380–392.

Hill, R.J., and Sternberg, P.W. (1993). Cell fate patterning during C. elegans vulval development. Development *18*, 9–18.

Hirabayashi, Y. (2004). The Wnt/ -catenin pathway directs neuronal differentiation of cortical neural precursor cells. Development *131*, 2791–2801.

Hudson, C., Kawai, N., Negishi, T., and Yasuo, H. (2013). B-Catenin-Driven Binary Fate Specification

Segregates Germ Layers in Ascidian Embryos. Curr. Biol. *23*, 491–495.
Huelsz-Prince, G., and van Zon, J.S. (2017). Canalization of C. elegans Vulva Induction against Anatomical Variability. Cell Syst. *4*, 219–230.e6.
Katsanos, D., Koneru, S.L., Mestek Boukhibar, L., Gritti, N., Ghose, R., Appleford, P.J., Doitsidou, M., Woollard, A., van Zon, J.S., Poole, R.J., et al. (2017). Stochastic loss and gain of symmetric divisions in the C. elegans epidermis perturbs robustness of stem cell number.
Kearns, D.B., and Losick, R. (2005). Cell population heterogeneity during growth of Bacillus subtilis. 3083–3094.
Koh, K., Peyrot, S.M., Wood, C.G., Wagmaister, J.A., Maduro, M.F., Eisenmann, D.M., and Rothman, J.H. (2002). Cell fates and fusion in the C. elegans vulval primordium are regulated by the EGL-18 and ELT-6 GATA factors -- apparent direct targets of the LIN-39 Hox protein. Development *129*, 5171–5180.
Korswagen, H.C. (2002). Canonical and non-canonical Wnt signaling pathways in Caenorhabditis elegans: Variations on a common signaling theme. BioEssays *24*, 801–810.
Korswagen, H.C., Herman, M. a, and Clevers, H.C. (2000). Distinct beta-catenins mediate adhesion and signalling functions in C. elegans. Nature *406*, 527–532.
Lin, R., Hill, R.J., and Priess, J.R. (1998). POP-1 and anterior-posterior fate decisions in C. elegans embryos. Cell *92*, 229–239.
Lindström, N.O., Lawrence, M.L., Burn, S.F., Johansson, J.A., Bakker, E.R.M., Ridgway, R.A., Chang, C.H., Karolak, M.J., Oxburgh, L., Headon, D.J., et al. (2014). Integrated β-catenin, BMP, PTEN, and Notch signalling patterns the nephron. Elife *3*, e04000.
Losick, R., and Desplan, C. (2008). Stochasticity and Cell Fate. Science (80-.). *320*, 65–68.
Maamar, H., Raj, A., and Dubnau, D. (2007). Noise in Gene Expression Determines Cell Fate in Bacillus subtilis. Science (80-.). *317*, 526–529.
Maloof, J.N., and Kenyon, C. (1998). The Hox gene lin-39 is required during C. elegans vulval induction to select the outcome of Ras signaling. Development *125*, 181–190.
Maloof, J.N., Whangbo, J., Harris, J.M., Jongeward, G.D., and Kenyon, C. (1999). A Wnt signaling pathway controls hox gene expression and neuroblast migration in C. elegans. Development *126*, 37–49.
Mentink, R.A., Middelkoop, T.C., Rella, L., Ji, N., Tang, C.Y., Betist, M.C., van Oudenaarden, A., and Korswagen, H.C. (2014). Cell intrinsic modulation of Wnt signaling controls neuroblast migration in C. elegans. Dev. Cell *31*, 188–201.
Mila, D., Calderon, A., Baldwin, A.T., Moore, K.M., Watson, M., Phillips, B.T., and Putzke, A.P. (2015). Asymmetric Wnt Pathway Signaling Facilitates Stem Cell-Like Divisions via the Nonreceptor Tyrosine Kinase FRK-1 in Caenorhabditis elegans. *201*, 1047–1060.
Mohler, W. a, Shemer, G., del Campo, J.J., Valansi, C., Opoku-Serebuoh, E., Scranton, V., Assaf, N., White, J.G., and Podbilewicz, B. (2002). The type I membrane protein EFF-1 is essential for developmental cell fusion. Dev. Cell *2*, 355–362.
Moss, E.G. (2007). Heterochronic Genes and the Nature of Developmental Time. Curr. Biol. *17*, 425–434.
Mucenski, M.L., Wert, S.E., Nation, J.M., Loudy, D.E., Huelsken, J., Birchmeier, W., Morrisey, E.E., and Whitsett, J.A. (2003). B-Catenin Is Required for Specification of Proximal/Distal Cell Fate During Lung Morphogenesis. J. Biol. Chem. *278*, 40231–40238.
Myers, T.R., and Greenwald, I. (2007). Wnt signal from multiple tissues and lin-3/EGF signal from the gonad maintain vulval precursor cell competence in Caenorhabditis elegans. Proc. Natl. Acad. Sci. U. S. A. *104*, 20368–20373.
Natarajan, L., and Eisenmann, D.M. (2002). Characterizing bar-1 function and regulation during C. elegans vulval development. East Coast Worm Meet.
Ohyama, T. (2006). Wnt signals mediate a fate decision between otic placode and epidermis. Development *133*, 865–875.
Park, F.D., and Priess, J.R. (2003). Establishment of POP-1 asymmetry in early C. elegans embryos.

Development *130*, 3547–3556.
Pénigault, J.B., and Félix, M.A. (2011a). Evolution of a system sensitive to stochastic noise: P3.p cell fate in Caenorhabditis. Dev. Biol. *357*, 419–427.
Pénigault, J.B., and Félix, M.A. (2011b). High sensitivity of C. elegans vulval precursor cells to the dose of posterior Wnts. Dev. Biol. *357*, 428–438.
Podbilewicz, B., Leikina, E., Sapir, A., Valansi, C., Suissa, M., Shemer, G., and Chernomordik, L. V. (2006). The C. elegans Developmental Fusogen EFF-1 Mediates Homotypic Fusion in Heterologous Cells and In Vivo. Dev. Cell *11*, 471–481.
Raj, A., van den Bogaard, P., Rifkin, S.A., van Oudenaarden, A., and Tyagi, S. (2008). Imaging individual mRNA molecules using multiple singly labeled probes. Nat. Methods *5*, 877–879.
Raj, A., Rifkin, S. a, Andersen, E., and van Oudenaarden, A. (2010). Variability in gene expression underlies incomplete penetrance. Nature *463*, 913–918.
Roiz, D., Escobar-Restrepo, J.M., Leu, P., and Hajnal, A. (2016). The C. elegans hox gene lin-39 controls cell cycle progression during vulval development. Dev. Biol. *418*, 124–134.
Roorda, A., and Williams, D.R. (1999). The arrangement of the three cone classes in the living human eye. Nature *397*, 520–522.
Salser, S.J., Loer, C.M., and Kenyon, C. (1993). Multiple HOM-C gene interactions specify cell fates in the nematode central nervous system. Genes Dev. *7*, 1714–1724.
Sarov, M., Murray, J.I., Schanze, K., Pozniakovski, A., Niu, W., Angermann, K., Hasse, S., Rupprecht, M., Vinis, E., Tinney, M., et al. (2014). A genome scale resource for in vivo tag-based protein function exploration in C. elegans. *150*, 855–866.
Sawa, H., and Korswagen, H.C. (2013). Wnt signaling in C. elegans. WormBook 1–30.
Schlager, B., Röseler, W., Zheng, M., Gutierrez, A., and Sommer, R.J. (2006). HAIRY-like Transcription Factors and the Evolution of the Nematode Vulva Equivalence Group. Curr. Biol. *16*, 1386–1394.
Shemer, G., and Podbilewicz, B. (2002). LIN-39 / Hox triggers cell division and represses vulval cell fusion. Genes Dev. *16*, 3136–3141.
Shemer, G., Suissa, M., Kolotuev, I., Nguyen, K.C., Hall, D.H., and Podbilewicz, B. (2004). EFF-1 is sufficient to initiate and execute tissue-specific cell fusion in C. elegans. Curr Biol *14*, 1587–1591.
Shetty, P., Lo, M.-C., Robertson, S.M., and Lin, R. (2005). C. elegans TCF protein, POP-1, converts from repressor to activator as a result of Wnt-induced lowering of nuclear levels. Dev. Biol. *285*, 584–592.
Smallwood, P.M., Wang, Y., and Nathans, J. (2002). Role of a locus control region in the mutually exclusive expression of human red and green cone pigment genes. Proc. Natl. Acad. Sci. U. S. A. *99*, 1008–1011.
Smurova, K., and Podbilewicz, B. (2016). RAB-5- and DYNAMIN-1-Mediated Endocytosis of EFF-Fusogen Controls Cell-Cell Fusion. Cell Rep. *14*, 1517–1527.
Sternberg, P.W. (2005). Vulval development. WormBook 1–28.
Sternberg, P.W., and Horvitz, H.R. (1986). Pattern formation during vulval development in C. elegans. Cell *44*, 761–772.
Wang, B.B., Müller-Immergluck, M.M., Austin, J., Robinson, N.T., Chisholm, A., and Kenyon, C. (1993). A homeotic gene cluster patterns the anteroposterior body axis of C. elegans. Cell *74*, 29–42.
Wernet, M.F., Mazzoni, E.O., Çelik, A., Duncan, D.M., Duncan, I., and Desplan, C. (2006). Stochastic spineless expression creates the retinal mosaic for colour vision. Nature *440*, 174–180.
Whangbo, J., and Kenyon, C. (1999). A Wnt signaling system that specifies two patterns of cell migration in C. elegans. Mol. Cell *4*, 851–858.
Wrischnik, L. a, and Kenyon, C.J. (1997). The role of lin-22, a hairy/enhancer of split homolog, in patterning the peripheral nervous system of C. elegans. Development *124*, 2875–2888.
Zeev-Ben-Mordehai, T., Vasishtan, D., Siebert, C.A., and Grünewald, K. (2014). The full-length cell-cell fusogen EFF-1 is monomeric and upright on the membrane. Nat. Commun. *5*, 3912.

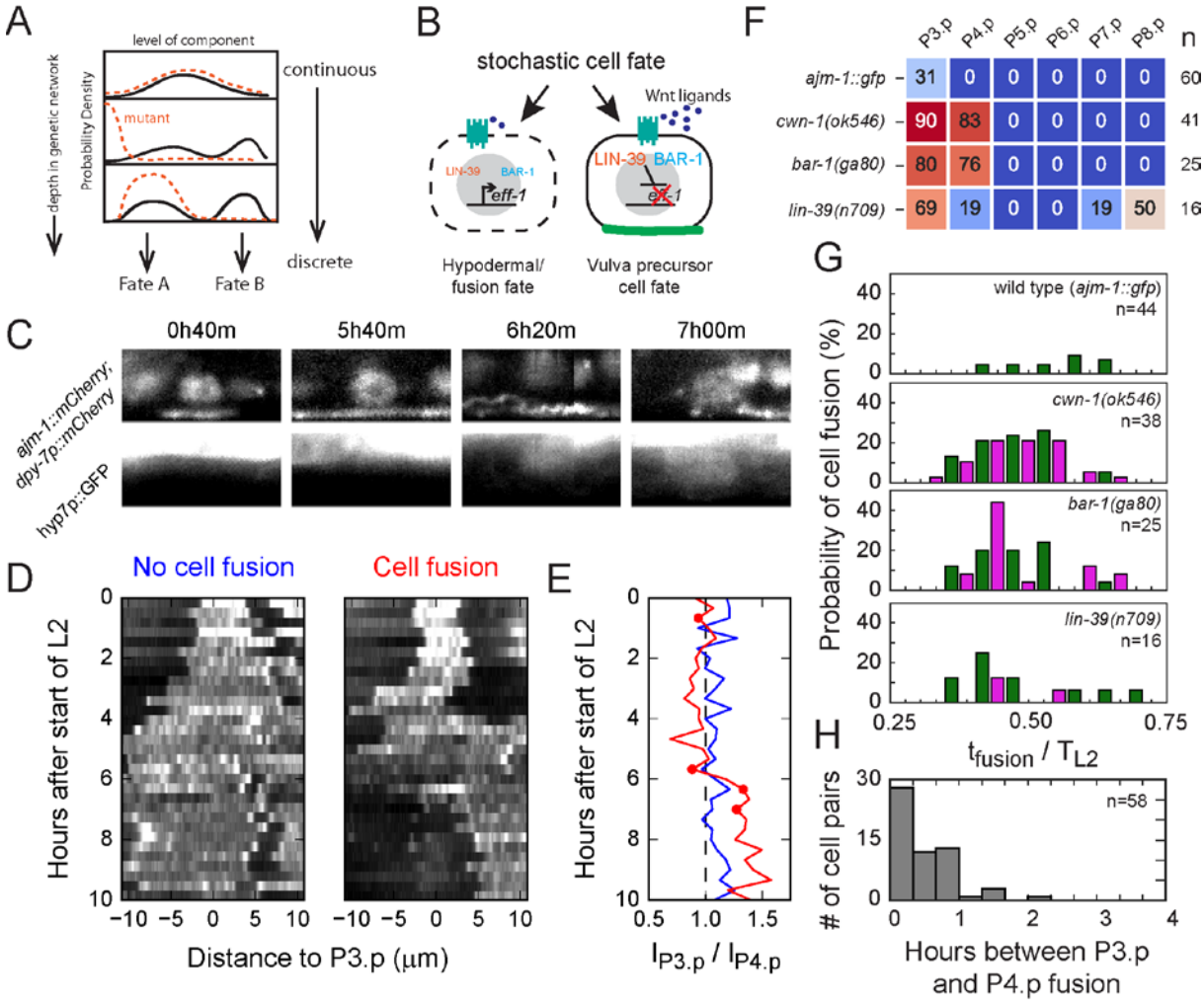

Figure 1. **Stochastic cell fate decisions in Pn.p cells.**

(A) Generic model of stochastic cell fate decisions. Continuous molecular noise is amplified by nonlinearities or feedback mechanisms in the underlying genetic network into bimodal variability (solid lines), with each peak in the bimodal distribution corresponding to a different cell fate. Relative frequency of cell fate can tuned by changing the distribution of continuous noise upstream in the signaling network (dashed lines). **(B)** Overview of the hyp7/fusion versus vulva precursor cell fate (VPC) decision. Cell assuming hyp7/fusion fate fuse (indicated by the dashed line) with the hypodermal syncytium hyp7 and lose the *ajm-1* apical junction marker (green). Cell fusion requires the expression of the fusogen *eff-1* and is inhibited by the Hox protein LIN-39 and by Wnt signaling through the β-catenin BAR-1. **(C)** Fusing P3.p cell carrying a nuclear marker (*dpy-7p;mCherry*). Upon fusion, the apical junction marker *ajm-1* retracts and GFP expressed in the hypodermal syncytium hyp7 flows into the cell. Scale bar, 5μm. **(D)** Kymograph of *ajm-1 ::mCherry* fluorescence along the anteroposterior axis in a P3.p cell that assumes VPC (left panel) and hyp7/fusion fate (right panel, corresponding to the cell in **C**). In both panels, *ajm-1* expressed in P4.p is visible on the right. **(E)** Comparing GFP inflow from the hyp7 syncytium in fusing and non-fusing cells. Shown is the ratio of GFP fluorescence intensity I between P3.p

and P4.p in the same animal. The blue and red line corresponds to the non-fusing and fusing cell in **D**, respectively. Red markers correspond to the time point shown in **C**. (F) Overview of measured hyp7/fusion frequencies in Pn.p cells in different mutant backgrounds. Mutants also carried the *ajm-1::gfp* reporter. **(G)** Distribution of cell fusion times of P3.p (green) and P4.p cells (magenta) in different mutant backgrounds. Mutants also carried the *ajm-1::gfp* reporter, used to determine the time of fusion. Time is expressed as fraction of the L2 larval stage duration T_{L2}. (H) Distribution of difference in cell fusion time between P3.p and P4.p cells, as measured in *cwn-1(ok546)*, *bar-1(ga80)* and *lin-39(n709)* mutant animals where both cells fuse.

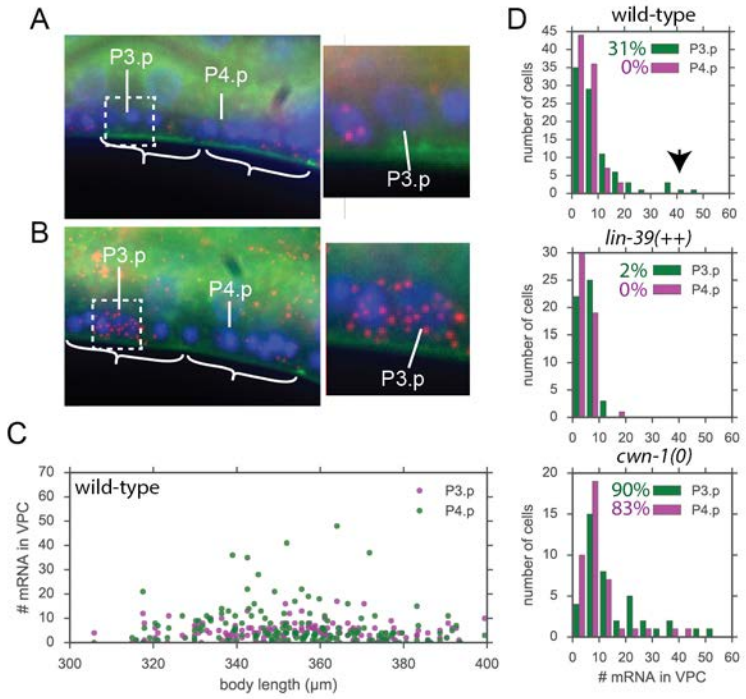

Figure 2. **Stochastic eff-1 expression in Pn.p cells.**

(A) Representative example of *eff-1* mRNA expression preceding cell fusion in a wild-type animal . Animals were stained for single *eff-1* mRNA molecules (red), nuclei were visualized with DAPI (blue), while the cell fate is monitored with *ajm-1::gfp* (green). White brackets indicate intact apical junctions/AJM-1::GFP, indicating that P3.p and P4.p have not yet fused. High levels of *eff-1* mRNAs were detected in the P3.p cell region, but were absent in the P4.p cell. The image was made by merging multiple z-stacks into a single merged image. **(B)** Similar to **B**, but a separate animal of similar age that has no apparent expression of *eff-1* mRNAs in the P3.p cell region. **(C)** Number of *eff-1* spots as a function of worm length (as a proxy for age), considering only unfused cells. The *eff-1* transcript is found to be occasional highly expressed in P3.p, while P4.p remains lowly expressed. The relatively few highly expressing P3.p cells suggests that fusion proceeds rather quickly after *eff-1* expression. **(D)** Histograms of the distribution of the number of *eff-1* spots in unfused P3.p and P4.p cells in different mutants, considering only times when the cell fate decision is close to taking place (P2.p cell expressing >10 *eff-1* mRNAs). The distributions of observed *eff-1* expression are altered in mutants with different fusion fate frequencies. Fusion frequencies of each cell are indicated in the legend of each histogram.

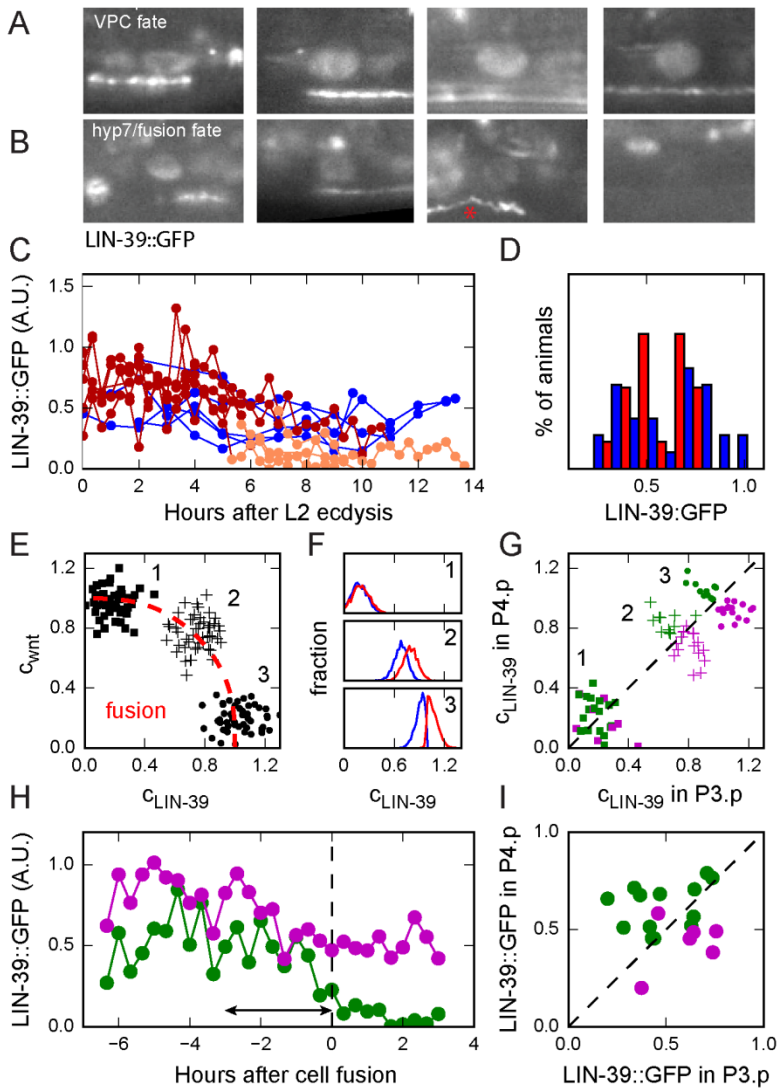

Figure 3**. Variability in LIN-39 protein level.**

(A), (B) Image sequence of cell assuming (A) VPC and (B) hyp7/fusion fate. Nuclear LIN-39 levels are visualized using a LIN-39::GFP protein fusion, while cell fusion is determined using an AJM-1::GFP reporter. The red star indicates the first time point at which AJM-1 retraction occurs, indicating that cell fusion has occurred. **(C)**. Nuclear LIN-39 fluorescence in fusing (red) and non-fusing (blue) P3.p cells. For fusing P3.p cells, color distinguishes time point prior to (dark red) and after fusion (light red). **(D)** Distribution of nuclear LIN-39 fluorescence in fusing (red) and non-fusing (blue) P3.p cells. In fusing cells, fluorescence was averaged over 3 hour window directly prior to fusion, whereas in non-fusing cells a time window of 3 hours prior to the average time of cell fusion was used. **(E)**. Model of inhibition of eff-1 expression and hyp7/fusion fate by Wnt signaling and LIN-39 (Eq. 1 in Methods). Fusion occurs in the region (indicated by the dashed red line) with sufficiently low Wnt signaling (c_{wnt}) and LIN-39 levels ($c_{\mathrm{LIN\text{-}39}}$). Markers are individual simulations of three scenarios, where (1) the cell fate decision is dominated by variability in Wnt levels (squares), (2) equally impacted by variability in Wnt and LIN-39 levels

(crosses), or (3) dominated by variability in LIN-39 levels (circles). **(F)** Distribution of LIN-39 levels in the model for cells that fuse (red) or assume VPC fate (blue), for each of the scenarios in (E). **(G)** LIN-39 levels in P3.p and P4.p for simulations in which P3.p assumes hyp7/fusion fate and the P4.p assumes VPC fate (green) or the reverse (magenta), for each of the scenarios in (E). **(H)** Nuclear LIN-39 fluorescence in P3.p (green) and P4.p (magenta) in an animal in which P3.p, but not P4.p, assumes hyp7/fusion fate. The arrow indicates the time window over which LIN-39 fluorescence is averaged in (D) and (I). The dashed line indicates the time of fusion. **(G)** Nuclear LIN-39 fluorescence levels in P3.p and P4.p for animals in which P3.p assumes hyp7/fusion fate and the P4.p assumes VPC fate (green) or the reverse (magenta). Each marker corresponds to a single animal and is averaged over a 3h time window prior to cell fusion.

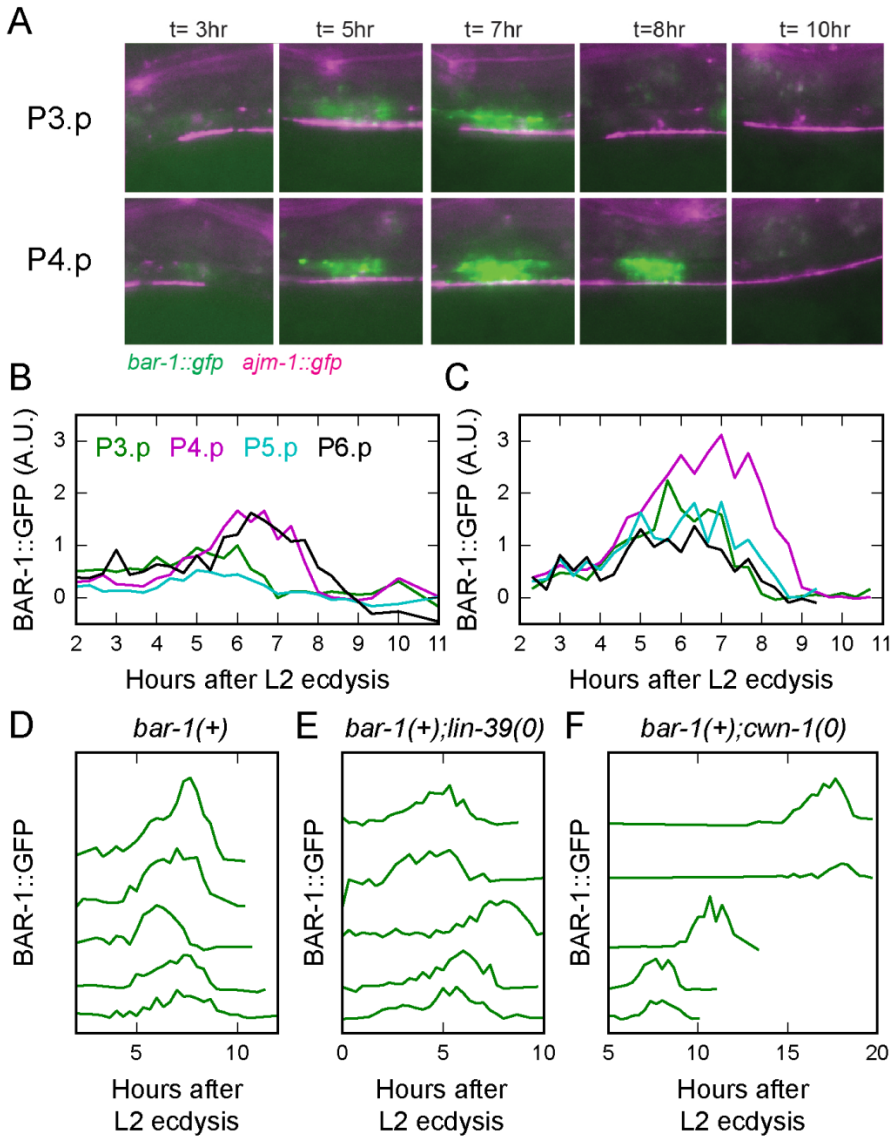

Figure 4. **Pulsatile BAR-1 dynamics during cell fate decision.**

(A) Image sequence of the BAR-1::GFP dynamics (green) over time in P3.p and P4.p cells in the same animal, with both cells assuming VPC fate. Animals also carry the *ajm-1::mCherry* marker (magenta). **(B),(C)** Dynamics of cellular BAR-1::GFP fluorescence in P(3-6).p cells in two different animals. **(D)-(F)** BAR-1::GFP dynamics in P3.p cells in (D) *bar-1(++)*, (E) *bar-1(++);lin-39(lf)*, (F) *bar-1(+); cwn-1(0)* animals. Traces for different animals are shifted along the vertical axis for clarity.

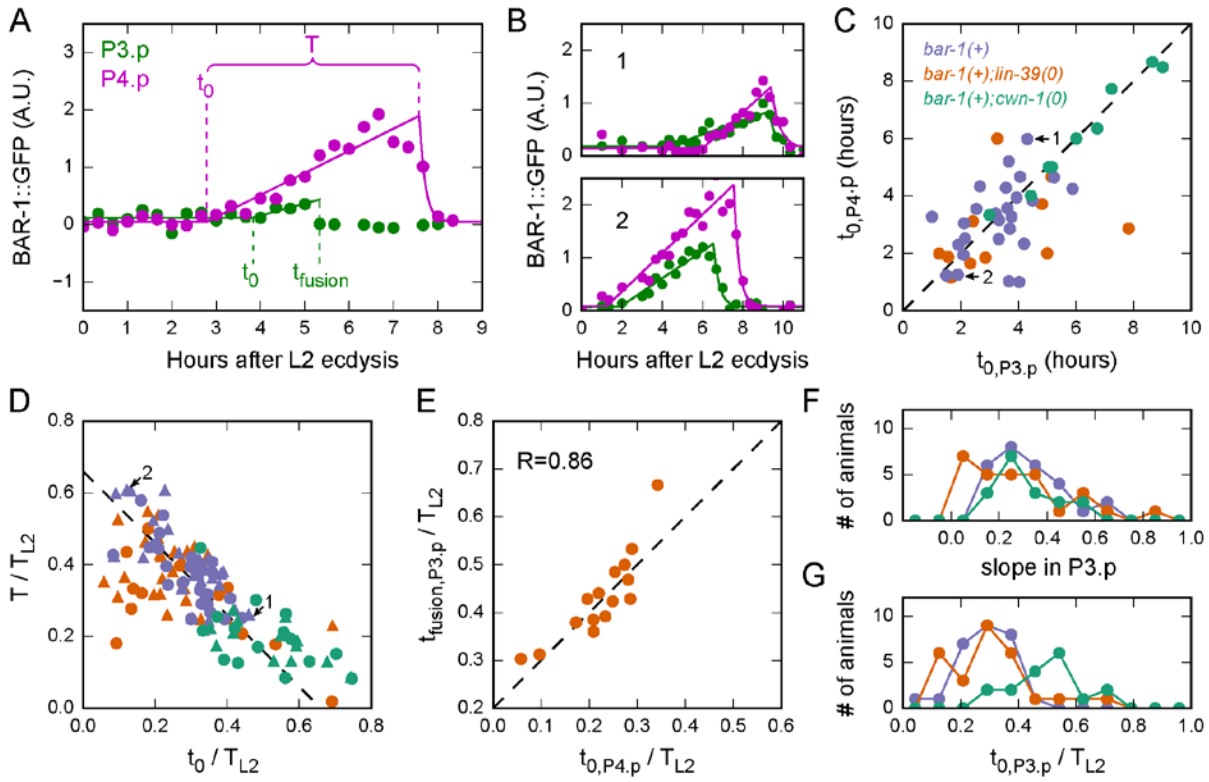

Figure 5. **Variability in BAR-1 pulse dynamics.**

(A) Quantifying BAR-1 pulse dynamics. Marker correspond to measured BAR-1::GFP levels in P3.p (green) and P4.p (magenta) for an animal in which P3.p, but not P4.p, assumes hyp7/fusion fate. Solid lines represent a model of BAR-1 accumulation dynamics (Eq. 3 in the Methods). Using the model, each BAR-1 accumulation pulse can be described hy three key parameters: pulse onset time t_0, pulse slope s and pulse duration T (for non-fusing VPCs) or time of fusion t_{fusion} (for hyp7/fusion cells). **(B)** Examples of animals showing differences in (relative) timing of BAR-1 accumulation pulses. **(C)** Correlation in pulse onset time t_0 between P3.p and P4.p cells in the same animal. Each marker corresponds to a single animal, with color indicating *bar-1(++)* (purple), *bar-1(++);lin-39(lf)* (orange) and *bar-1(++);cwn-1(0)* mutants (cyan). Animals were selected where neither P3.p nor P4.p fused. Arrows indicate the animals in (B). **(D)** Correlation between pulse onset time t_0 and pulse duration T in non-fusing P3.p (circles) and P4.p cells (triangles). Color indicates the different mutant backgrounds in (C) and arrows indicate the animals in (C). Time is expressed as fraction of the L2 larval stage duration T_{L2}. The dashed line is $T/T_{\text{L2}} = 0.66 - t_0/T_{\text{L2}}$. **(E)** Correlation between pulse onset time t_0 in P4.p and fusion time t_{fusion} in P3.p, in *bar-1(++);lin-39(lf)* animals where P3.p, but not P4.p, assume hyp7/fusion fate. The dashed line is $t_{\text{fusion}}/T_{\text{L2}} = 0.2 + t_0/T_{\text{L2}}$. **(F), (G)** Distribution of (F) pulse onset time t_0 and (G) pulse slope s in P3.p cells. Color indicates the different mutant backgrounds in (C). Data for P3.p cells that assume hyp7/fusion and VPC fate is pooled.

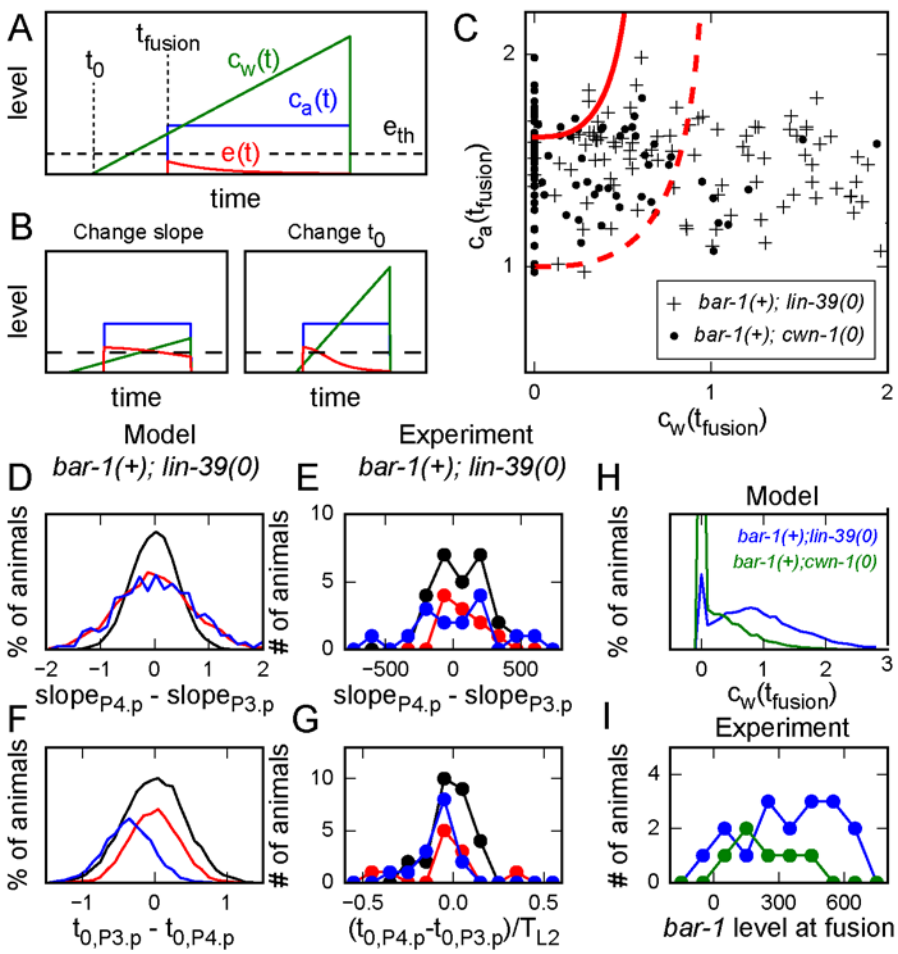

Figure 6. **Cell fate bias by BAR-1 pulse dynamics.**

(A) Model of inhibition of *eff-1* expression level $e(t)$ (red line) and hyp7/fusion fate by a pulsatile Wnt signaling level $c_{\mathrm{wnt}}(t)$ (green line) (Eq. 2 in Methods). Cell fusion is activated at time t_{fusion}, but only occurs if the activation level c_a (blue line) is high enough and the Wnt inhibition $c_{\mathrm{wnt}}(t)$ is low enough that *eff-1* is expressed above a threshold level e_{th} (dashed line). **(B)** In this model, fusion frequency can be changed both by changing the slope (left panel) and onset time (right panel) of BAR-1 pulses. **(C)** Model simulations of cell fate decisions in different mutant backgrounds. For wild-type animals, hyp7/fusion fate occurs in a small region (demarcated by the solid red line). Upon removal of the inhibitor LIN-39 this region is expanded (dashed red line). Crosses correspond to individual simulations for animals with elevated BAR-1 levels (*bar-1(++)* and *bar-1(++);lin-39(lf)*) and circles to simulations with BAR-1 levels closer to wild-type (*bar-1(++); cwn-1(0)*). **(D),(E)** Distribution of the difference in pulse slope s for BAR-1 pulses in P3.p and P4.p, both for the (D) model and (E) experiments. Shown are distributions for *bar-1(++)* animals (black line), where no Pn.p cells fuse, and *bar-1(++);lin-39(lf)* animals where P3.p, but not P4.p, fused (blue line) or where neither P3.p nor P4.p fused (red line). In all cases, pulse slope does not bias the cell fate decision. **(F),(G)** Distribution of the difference in pulse onset time t_0 for BAR-1 pulses in P3.p and P4.p, both for the (F) model and (G) experiments. Line color indicates mutant background as in (D) and (E). For the experimental data, time is

expressed as fraction of the L2 larval stage duration T_{L2}. Late pulse onset biases towards hyp7/fusion fate. **(H), (I)** Comparing BAR-1 levels at the time of cell fusion between *bar-1(++);lin-39(lf)* (blue) and *bar-1(++);cwn-1(0)* animals (green), both for the (H) model and (I) experiments. For the experiments, data for P3.p and P4.p cells was pooled. BAR-1 levels at time of fusion are higher in *bar-1(++);lin-39(lf)* animals.